Eur. Phys. J. Plus (2025) 140:347
https://doi.org/10.1140/epjp/s13360-025-06282-4

THE EUROPEAN
PHYSICAL JOURNAL PLUS

Regular Article

Capillary water uptake in artificially weathered geopolymers for cultural heritage conservation: real-time neutron imaging investigation

Maria Cristina Caggiani[1], **Filomena Salvemini**[2], **Claudio Finocchiaro**[1], **Maura Fugazzotto**[1], **Roberta Occhipinti**[1], **Silvia Portale**[1], **Sabrina Zafarana**[1], **Paolo Mazzoleni**[1,a], **Germana Barone**[1]

[1] Department of Biological, Geological and Environmental Sciences, University of Catania, C.so Italia 57, Catania, Italy
[2] Australian Nuclear Science and Technology Organisation, New Illawara Road, Lucas Heights, NSW 2232, Australia

Received: 12 November 2024 / Accepted: 29 March 2025

Abstract This work involved the use of neutron imaging for the study of the mechanism and rate of capillary water uptake within alkali-activated materials (geopolymers) synthesized starting from natural and industrial waste precursors of the Sicilian territory, to be applied to the conservation of cultural heritage. In detail, the materials were produced starting from Mt. Etna Volcanic ash, basalt cutting sludges and industrial ceramic tiles wastes; the starting formulations were also enriched with different types of additives (calcium-rich or reinforcing fibres); furthermore, all the samples were investigated both as such and after preliminary weathering treatment inducing sodium chloride crystallization. The aqueous solutions transfer capability of the products was investigated, with important implications in the possible formation of efflorescence. This is vital when prospecting a conservation intervention and evaluating the suitability of the materials for this scope. The study during water uptake was conducted by means of neutron radiography continuously acquiring images integrated on 10 s, while the wet samples of the ceramic-based geopolymers group were studied also by means of neutron tomography with the aim of observing the porous structures/the formed fractures in 3 dimensions. The data were treated and the sorptivity of the materials was obtained, giving some indications about the advisable formulations (e.g. with calcium-based additive) and those to be avoided for cultural heritage conservation (e.g. ceramic-based without additive).

1 Introduction

With increasing global concerns over CO_2 emissions, there has been a significant tendency towards exploring alternative solutions in the construction industry, with geopolymers belonging to the group of alkali-activated materials emerging as a particularly promising line of research. Considered as low-carbon substitutes for Portland cement, they have garnered considerable attention [1, 2]. These materials can be produced at room temperature by mixing aluminosilicate powders with an alkaline activator such as sodium hydroxide and/or sodium silicate solutions. A given combination of silicon, aluminium and cations from the precursors and the alkaline solution initiates the reaction, resulting in a new geopolymerized inorganic product. Aluminosilicate powder can be derived from various sources, both natural and synthetic. Consequently, the possibility of using natural and industrial by-products such as volcanic ash, stone cutting sludges or ceramic wastes increases the attractiveness of these products, aligning them closely with sustainable materials development goals [3]. Moreover, the suitability of these materials for cultural heritage conservation is currently under investigation [4].

An important, still open, question concerns geopolymers durability due to weathering action, including the possible formation of efflorescence and sub-efflorescence due to an excess of Na^+ after the polycondenzation reaction [5, 6]. Specifically, the reaction between the exceeding Na^+ and the CO_2 of the atmosphere, known as carbonation, leads to the formation of new crystal species, i.e. sodium carbonates. These latter significantly affect the pore structure with possible occurrence of micro-cracking and breaking up of the initial material's structure [7]. This deterioration process is mainly due to the chemical unbalance between the components of the geopolymer system (i.e. the starting material and the quantity of alkaline solution used in the formulation). As a consequence, it is important to study the materials composition, the porosity and its distribution in association with water penetration, a physical process that can directly influence geopolymers service life and durability [8, 9].

The neutrons interaction with matter makes them an ideal tool for studying not only the structural properties of the materials, but also geopolymers interaction with penetrating water, thanks to high neutrons cross section of H. The capillary water uptake in cement-based materials is studied by means of neutron imaging [8, 10–16] and first attempts to use this technique for geopolymers have been made on fly ash-based products [9] and on metakaolin (MK) and slag-based ones reinforced with steel fibres [17], with the main aim of assessing their properties, in association with mechanical performance, as building materials. A recent study on fly

---

[a] e-mail: paolo.mazzoleni@unict.it (corresponding author)

Table 1 Details of the geopolymer formulations studied in this work

Group	Code		Precursor/MK (wt% / wt%)	NaOH (8 M)/Na_2SiO_3	Na_2SiO_3 (SiO_2/Na_2O molar ratio)	Additive	L/S ratio
	Non weathered	Weathered					
Volcanic ash	VM20	VM20_S	4.00	0.32 (+ 5.3 wt% H_2O)	2	–	0.32
	VM20GR	VM20GR_S	4.00	0.32 (+ 5.3 wt% H_2O)	2	Slaked lime	0.32
	VM20CAR	VM20CAR_S	4.00	0.32 (+ 5.3 wt% H_2O)	2	Carbon fibre	0.32
Basaltic cutting sludges	FB40	FB40_S	4.00	0.82	3	–	0.4
	FBC40	FBC40_S	4.00	0.82	3	Aluminium-rich cement	0.4
Ceramic waste	LBCa1-1 + 10MK	LBCa1-1 + 10MK_S	9.00	1.00	3	–	0.4
	LBCa 1–1 + 10MK-P	LBCa 1–1 + 10MK-P_S	9.00	1.00	2	Prompt	0.3

ash-based geopolymers validated the effectiveness of using neutron radiography as a non-destructive technique to assess the pore and water distribution within the samples [18]. Moreover, other scientists employed neutron imaging for studying the carbonation depth of geopolymers [19]. Analogous neutron studies in the field of cultural heritage were instead conducted on capillary water uptake of natural building stones [20], and on the application and penetration of consolidants in these types of materials [21–24].

Capillary water uptake and the water distribution within the samples are mainly controlled by the material's microstructure, including total porosity, type of porosity (i.e. closed or open), pore size and distribution. Nowadays, many techniques, both destructive and non-destructive, allow the understanding of these features. In particular, methods such as Mercury Intrusion Porosimetry (MIP), nitrogen adsorption, Scanning Electron Microscopy (SEM), Transmission Electron Microscopy (TEM), and X-ray Computed Tomography (XCT) have been used to investigate the microstructure of construction materials, including geopolymers, offering precious information on how the porosity influences the water uptake, the durability and the final performances of the samples [25–27]. However, neutron imaging can be additionally employed as an effective and non-destructive method to further understand the evolution of the waterfront during capillary water uptake and to gain deeper knowledge on the discussed features [28]. Hence, the combined study of composition, pore structure and transport mechanisms become crucial for the design of geopolymers for cultural heritage conservation application. This work aims at exploiting the benefits of neutron imaging study during capillary water uptake of geopolymers made with waste Sicilian (Italy) raw materials, under test of employment in conservation sites, and fully characterized from a chemical and mineralogical point of view. Geopolymer binders, based on Sicilian volcanic and industrial waste materials, will be tested, also with the supplement of additives and with reinforcing carbon fibres. Some replicates of the samples will be subjected to artificial weathering by means of exposition to salts crystallization. By means of real-time neutron radiography, we will focus on the mechanism of water filling the pores and the possible cracks, comparing the behaviour of the various precursors, the various formulations with and without additives, and the effect of salt crystallization, in view of their use for cultural heritage conservation. Some tests of neutron tomography after imbibition will be also carried out with the aim of three dimensionally evaluating the pores and fractures systems.

2 Materials and methods

2.1 Samples

Three groups of geopolymers (Table 1) were synthesized based on: Mt. Etna volcanic ash; basalt cutting sludges; ceramic waste. For each of the groups, a starting formulation was developed considering previous works (paragraph 2.1.1) and improved ones with different types of additives: Ca-based additive and/or carbon fibres (paragraph 2.1.2). Each of the seven resulting products was subjected to a laboratory test with salts crystallization (paragraph 2.1.3).

2.1.1 Starting formulations

The volcanic ash used for this work was collected from the 2013 eruption in the area of Santa Venerina, on the eastern slopes of Mount Etna (Sicily, Italy). The mineralogical and chemical composition of the ash can be found in previous studies [29, 30]. Before activation, the ash was washed and dry-milled to obtain a grain size fraction below 75 µm. The formulation used for this study was taken from [31] and [32].

Samples of basaltic cutting sludges, obtained from A.M. Basalti S.r.l. in Misterbianco (Sicily, Italy) were collected directly from outdoor heaps. At the moment of the sampling, these sludges were still wet, and thus, they underwent to a 24 h drying in oven at 100 ± 5 °C and were subsequently sieved using a series of meshes starting from 3 mm in diameter up to 50 µm to subtract any larger organic or inorganic particles, present due to the outdoor storage, from the basaltic cutting sludge. The geopolymeric formulation FB40, based on these rock cutting sludges and experimented by [33], was selected for this study.

Industrial tiles waste (labelled LBCa; provided by La Bottega Calatina arl—Caltagirone (CT), Italy) was used for producing ceramic-based geopolymers. Its chemical and mineralogical characterization is available in previous studies [34], as well as its thermogravimetric behaviour and its reactivity under alkaline conditions [35]. The ceramic tiles were grounded by porcelain jars reaching a grain size of about 10 µm. Details of the formulation are available in previous studies [34].

In all cases, variable fractions (see Table 1) of MK (ARGICALTM M-1000, provided by IMERYS, France) were added to the main precursor powders. The solids were mixed with liquid sodium hydroxide (NaOH, 8 M solution) and sodium silicate (Na_2SiO_3, provided by Ingessil s.r.l., Italy). All together they were mechanically mixed for 5 min, poured into 2 × 2 × 8 cm prismatic moulds in six replicates, and then mechanically vibrated to remove any air incorporated during mixing. The moulds were then sealed to maintain consistent moisture and temperature conditions for 48 h. After this period, the samples were unsealed and left to dry at room temperature until they reached 28 days of curing. Since MK is present in all the formulations, for the sake of brevity, the groups of samples will be defined with the name of the main precursor only. Details of all the formulations are reported in Table 1.

2.1.2 Geopolymers with additives

The VM20GR recipe was obtained by adding a small amount of slaked lime paste to the VM20 paste, in order to improve the physical–mechanical properties (e.g. setting time, mechanical strength and rheological features) useful for conservation works on vertical supports performed, e.g. at Monreale Cathedral (Palermo, Italia) [4], as experimentally demonstrated in [32].

FBC40 is an improved version of the FB40 formulation by incorporating a small weight fraction of a highly reactive powdered cement (C) rich in aluminium, aimed at limiting the formation of new sodium carbonate phases resulting from an excess of Na+ ions, a common phenomenon in alkali-activated materials. This excess cannot be avoided when the geopolymer's formulation is not stoichiometrically balanced [29]. The introduction of the aluminium-rich cement promotes the balance of Na^+ due to the presence of available aluminium in the gel system [36].

Moreover, 1 wt% of carbon fibres, provided by R&G Faserverbundwerkstoffe GmbH (Germany), were added to VM20 and FB40 formulations. Among all fibres, carbon ones are known to have higher resistance to corrosion in alkaline environments and not to take part in the activation reactions of the materials [37, 38]. The fibres were cut to a length of approximately 7 cm and then manually placed into the moulds during casting. The embedding of fibres followed a sandwich-like structure made of subsequent layers of geopolymer paste and fibres. The addition of fibres is proven to enhance durability and mechanical properties of samples, thus reducing the brittle behaviour [39].

A second ceramic-based geopolymer formulation was implemented by adding a calcium-based component (namely Prompt, supplied by Vicat Group–Paris, France). Details of the formulation are available in previous studies [40].

2.1.3 Weathering of the geopolymers

Salt crystallization resistance test was carried out on 3 of the 6 replicas according to the sequence of [41]. Some variations were made following alternative suggestions found in [42], substituting NaCl to $Na_2SO_4 \times 10H_2O$ and prisms (2 × 2 × 6 cm) to cubes (4 cm). The specimens were dried in oven at 105 ± 5 °C until constant mass was reached. These were then placed in separate sealed buckets, keeping approx. 2 cm distance from the sides, and immersed up to a height of approx. 1 cm above the specimen in a 14% sodium chloride (NaCl) solution. The samples were subjected to 15 cycles of immersion (2h), drying in oven at 105 ± 5 °C (12 h) and cooling (2 h) before being re-immersed in the fresh solution. At the end, they were removed from the oven and placed in water for 24 h at 23 °C and finally thoroughly rinsed in running water. The results are expressed as a relative difference in mass (ΔM) (i.e. loss or gain in mass).

$$\Delta M = \frac{M_f - M_d}{M_d} * 100 \tag{1}$$

where: M_f is the final dry mass; M_d is the dry mass before the first cycle.

2.2 Methods

The neutron imaging study was conducted at the DINGO beamline at the Australian Nuclear Science and Organisation (ANSTO) [43] to visualize the capillary water uptake in the set of geopolymers.

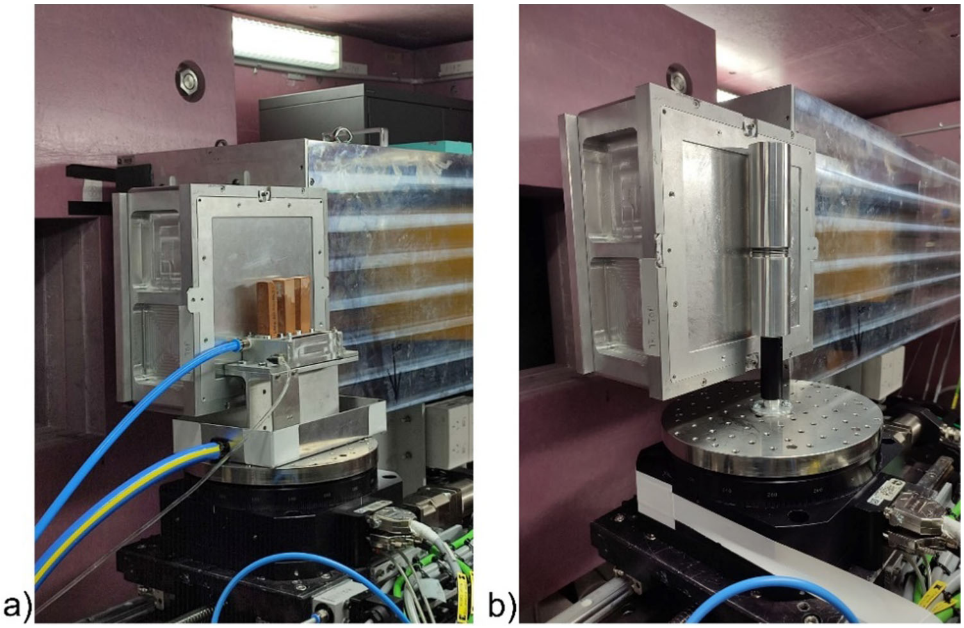

Fig. 1 Experimental set for the real-time radiographic measurement during imbibition with the three replicas of each sample (**a**) and of the tomographic scan with two samples stacked to be measured simultaneously (**b**)

The DINGO beamline was set in high intensity mode (with the ratio of collimator-detector length L to inlet collimator diameter D equals to 500). The detector system was configured with the ZWO ASI 2600MM PRO (6248 × 4176) CMOS camera, coupled with a 50 mm lens to achieve a pixel size of ~ 25 μm over a field of view of about 15.6 × 10.5 cm^2, and equipped with a 50 μm ^{6}LiF/ZSn scintillation screen. During the real-time radiographic measurement, three replicates of the same specimen type were positioned on a purposely designed and manufactured imbibition platform. The specimens were aligned in front of the detector and measured simultaneously (Fig. 1a). The diffusion of water into the sample was monitored by recording a sequence of radiographies each with an exposure time of 10 s for a total irradiation period ranging from 30 min to 8 h, depending on the observed water imbibition.

After the imbibition experiment, the three-dimensional distribution of the water front was investigated by rapid neutron tomography; hence, the migration of water due to evaporation could be considered negligible. In this case, the detector system was set to yield images with a pixel size of ~ 40 μm and equipped with a 100 μm ^{6}LiF/ZSn scintillation screen in order to widen the field of view (25.0 × 16.7 cm^2) and increase the light output for the transmitted neutron flux. The tomographic scan consisted of 372 projections, equiangularly distributed over a 360° range with an exposure time of 5 s at each step angle. Two specimens were stacked and measured simultaneously during the same scan (Fig. 1b). Only one selected sample for each type of geopolymer was measured due to time constrain.

The radiographic data were processed and evaluated using the software package ImageJ 1.54d. Flat field normalization with dry sample, dose correction and dark current subtraction were applied. The neutron intensity profile averaged across the sample width was measured along the sample length at different intervals of the radiographic acquisition (e.g. in Fig. 2). The inflection point of the profile curve, representing the boundary between darker grey (wet sample) and lighter grey (dry sample) indicated the water front, which was plotted against the squared root of the chosen times to obtain the sorptivity curves with an intercept fixed to zero [20]. For irregular fronts, the main inflection point has been considered.

The Octopus code was used for the tomographic reconstruction [44], and the obtained slices were recomposed and evaluated using the Avizo 2023.1 software [45].

3 Results

3.1 Capillary water uptake through neutron radiography

In the following sections, the groups of geopolymers synthesized with different precursors will be described and discussed separately to evaluate the effect of the additive/fibres and of the salt crystallization test on each formulation. Even though, for each sample, three replicates were measured, a representative one was selected to be shown in the contour maps images. With respect to grey scale (Fig. 2), this rendering is useful to better visualize the different water concentration according to an arbitrary scale from 0 (dry) to 1 (saturation) in the sections of the specimen. The time intervals are different and water rate of uptake cannot be compared observing these images, since each material was characterized by a different imbibition and a different time of saturation (Figs. 3, 5, 7). On the other hand, the times are the same as those chosen for the front position plots: these are indicative of the rate of water uptake in the

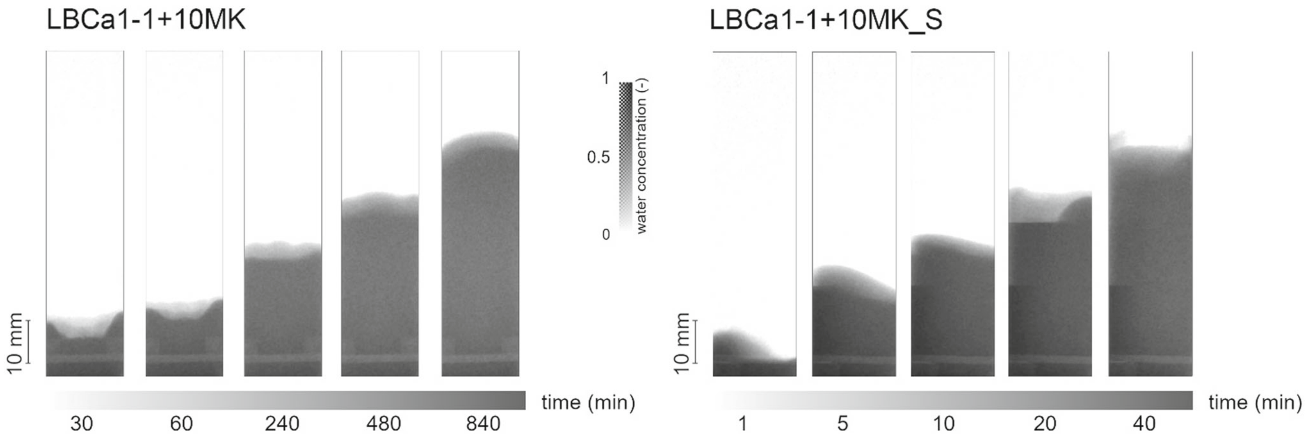

Fig. 2 Example of neutron radiographic sequences for samples LBCa 1–1 + 10MK and LBCa 1–1 + 10MK_S, respectively. At the bottom of each frame, the progression bar shows the time stamp selected. The grey scale in the middle indicates the correspondence between the grey tone and the relative concentration of water in the sample. As the grey tone depends on the amount of water, the same dynamic range normalized to an arbitrary scale from 0 (dry) to 1 (saturation) is applied to all samples

specimens; here, all the three replicates have been considered and the average with standard deviation values are shown (Figs. 4, 6, 8).

3.1.1 Volcanic ash-based geopolymers

The contour maps during water uptake at selected time intervals for all the volcanic ash-based products are shown in Fig. 3.

At a first view, it can be remarked that all the geopolymers show the highest concentration of water on one side of the specimen, indicating a preferential uptake from this specific side. Even though the shape of the front appears variable and tending to be flat after a given time (e.g. 300 min for VM20, 120 min for VM20GR and VM20GR_S), it results almost always inclined in the same direction. This side coincides with the long bottom side of the specimen in the mould and this phenomenon could be linked to a different intensity of compaction as suggested by [15]. Actually, the external side of the specimen, where the water is absorbed more slowly, is usually characterized by an accumulation of sodium silicate on the surface, due to the settlement of the solid particles, giving a typically shiny aspect [31]. This explains the higher compactness of this side; furthermore, it has been hypothesized that this layer is about 2 mm thick [31], which corresponds to the section which is avoided by most of the rising water. The extent of this phenomenon seems reduced in the weathered samples, especially for VMGR_S and VM20CAR_S. Probably, the salts crystallization treatment being isotropic—and depending on the pore distribution within the sample- it attacks the volcanic ash specimens on both sides in the same way, making the material penetrable to water more homogenously. On the other hand, the reason why the highest concentration of water remains on the basis of the sample might be searched in the salts partially occluding the porosity. Concerning samples VM20CAR and VM20CAR_S, the shape of the contours highlights the heterogeneity created by the fibres in the material. This is even better visible in VM20CAR_S, due to the cracks formed with salts crystallization causing discontinuities between the fibres and the geopolymer material, inducing water to be here preferentially absorbed. This is observed in literature in cement-based composites subjected to direct tension tests [13, 16].

In order to compare the rate of water absorption in the different cases, the front position was plotted against the square root of the time as described in paragraph 2.2. and the results are shown in Fig. 4.

As clear from the regression lines, the relationship is linear and the line slopes account for the sorptivity [9, 10, 20]. The coefficients of determination (R^2) are > 0.99, assuring a good fit of the regression lines. The lower rate of water absorption is by far that of the geopolymer with the addition of 2% of slaked lime (VM20GR). Recent studies demonstrated that this addition also improved the rheological properties, reduced the setting time of 70% and increased the mechanical performance of 30% with respect to VM20 [32]; furthermore, this formulation proved successful during the conservation tests carried out at the Monreale Cathedral (Italy) [4]. It is worth noting that the addition of fibres does not sensibly increase the water absorption rate. As carbon fibres are known to be hydrophobic [46], the capillary uptake of water takes place only along the transition zone between fibres and the matrix [47]. Moreover, the type and amount of fibre strongly affect this zone, resulting in a different bulk water absorption behaviour of the specimen [48]. The water absorption rate obtained for the samples with the addition of fibres might therefore suggest, notwithstanding the formation of some cracks, a good adhesion of the fibres with the volcanic ash matrix. In all cases, as expected, the sorptivity is higher for the weathered samples with respect to the fresh ones.

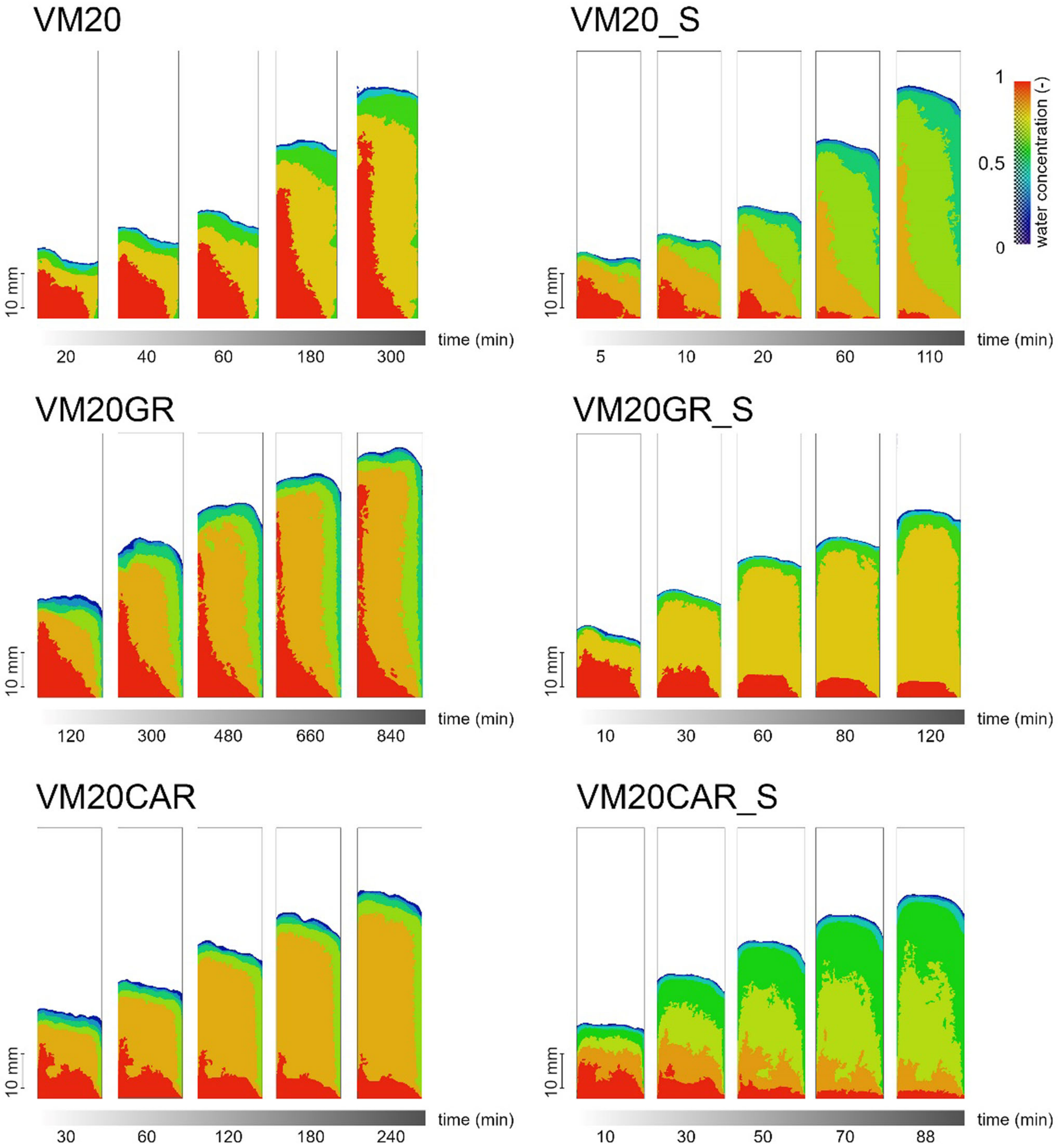

Fig. 3 Contour maps during water uptake of volcanic ash-based samples. At the bottom of each frame, the progression bar shows the time stamp selected. The colour map at the top right corner indicates the correspondence between the rendered colour and the relative concentration of water in the sample

3.1.2 Cutting sludges-based geopolymers

Contour maps of the water uptake for basaltic cutting sludges geopolymers at given times are shown in Fig. 5, and the respective water absorption rate plots in Fig. 6. Once again, the internal side of the prisms is that characterized by the areas with higher water concentration. In this case, the external side seems even less permeable to water than what observed for volcanic ash. FB40_S has no real preferential direction of water uptake, while in FBC40_S water rises in the very first millimetres of the internal side and is accumulated at the basis of the prism. The two latter are surely much influenced by the system of cracks formed after salts crystallization. In general, the shapes of the contour maps are more ragged than those observed for volcanic ash materials,

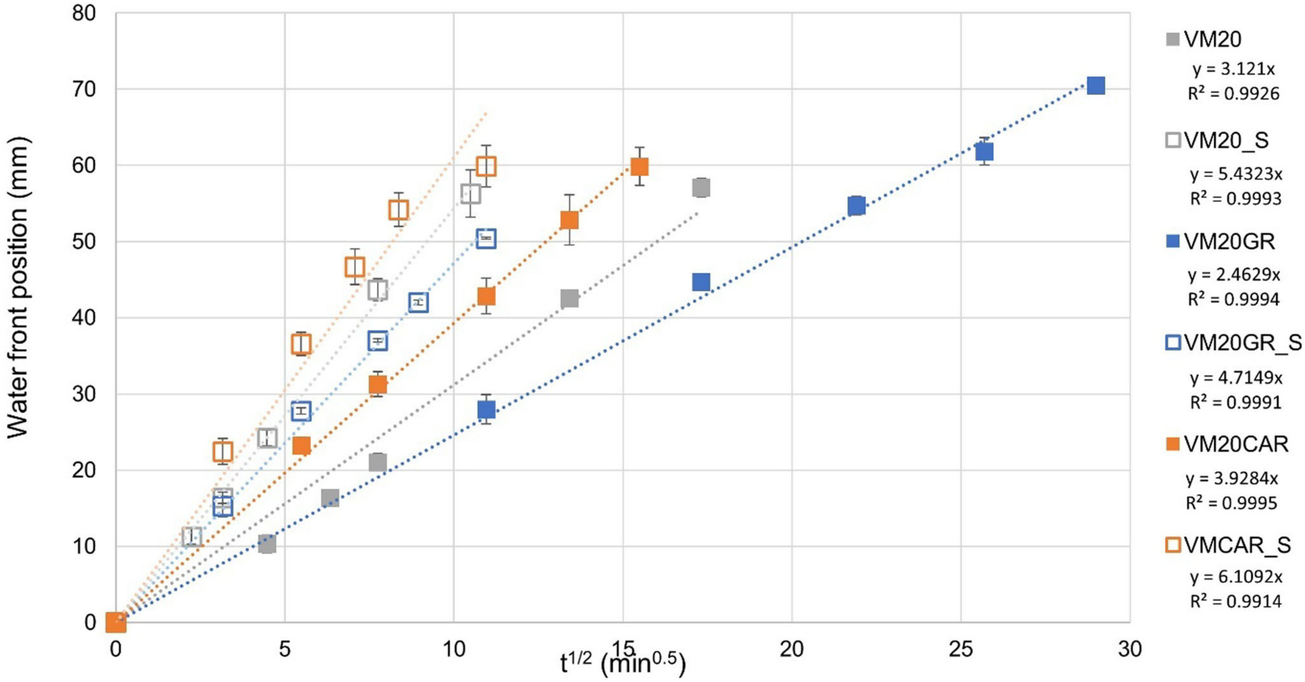

Fig. 4 Water front position as a function of the square root of time for volcanic ash-based samples

suggesting, especially for the weathered samples, that water follows a coarser porosity and cracks [20]. This finding may be justified by the presence of a polymodal pore size distribution which characterizes the geopolymers based on basaltic cutting sludge, both additivated and not (Finocchiaro-Portale, personal communication 2024); polymodal porosity would make the wave front jagged due to the heterogeneously sized porosity found during ascent. In contrast, volcanic ash-based geopolymers are characterized by a unimodal pore size distribution, which would allow the front of water to rise more regularly.

In this case, too, the formulation with the additive is that characterized by the lowest slope of the linear regression (Fig. 6), even though the difference with the respective starting formulation is here much reduced. This indicates that the same weight fraction of aluminium-rich cement addition to basaltic cutting sludges geopolymers has a minor impact effect with respect to the that of slake lime addition to volcanic ash ones, at least as far as the water uptake is concerned. This could be attributed to the fact that, according to previous studies, while the addition of slake lime to the volcanic ash formulation causes a significant reduction in open porosity of the starting formulation, the aluminium-rich additive hardly affects the open porosity of the basaltic sawing sludge starting formulation (Finocchiaro-Portale, personal communication 2024). The slight difference between the two formulations, with and without Al rich cement, is confirmed by the respective weathered ones, showing values that can be considered overlapped due to the error bars. The increase in sorptivity after the salts crystallization is instead evident in both cases. The lowest R^2 is that of FB40: actually, there is a slowing down of the water uptake registered with the measure at 420 min.

3.1.3 Ceramic waste-based geopolymers

Ceramic waste-based geopolymers behave quite differently from all the others. Contour maps of the water uptake are shown in Fig. 7 and the respective plots of front positions at the same moments are reported in Fig. 8. Except for LBCa 1–1 + 10MK_S, the other samples show a symmetric rise of the water, either from the middle of the prism (LBCa 1–1 + 10MK) or from the borders (the two formulations with additive). For the latter, this behaviour is expected, since, contrarily to what happens for all the other formulations, the typical slightly shiny surface due to the accumulation of sodium silicate is not observed here, therefore water can rise in the same way from both sides. It must be noticed, instead, how in LBCa 1–1 + 10MK, even after several hours of imbibition, the water remains mainly concentrated at the basis, where the prism is immersed, and it rises through the prism in much lower concentration. This is due to a mostly closed porosity or to pores interconnected by bottlenecks of sub-capillary dimensions.

The plots in Fig. 8 are quite interesting because they include the linear regression with the lowest slope (LBCa 1–1 + 10MK-P) and that with the highest one (LBCa 1–1 + 10MK_S), characterized at the same time by the highest standard deviation, of all the studied materials. The ceramic-based geopolymer with the natural hydraulic lime addition is that guaranteeing the slowest water absorption among all the formulations, probably due to a higher compactness. Even the respective weathered sample has a performance comparable with the non-weathered cutting sludges and volcanic ash ones. In fact, it is known from the literature that there is a correlation between the higher concentration of calcium in the mixture and the higher density and compactness of

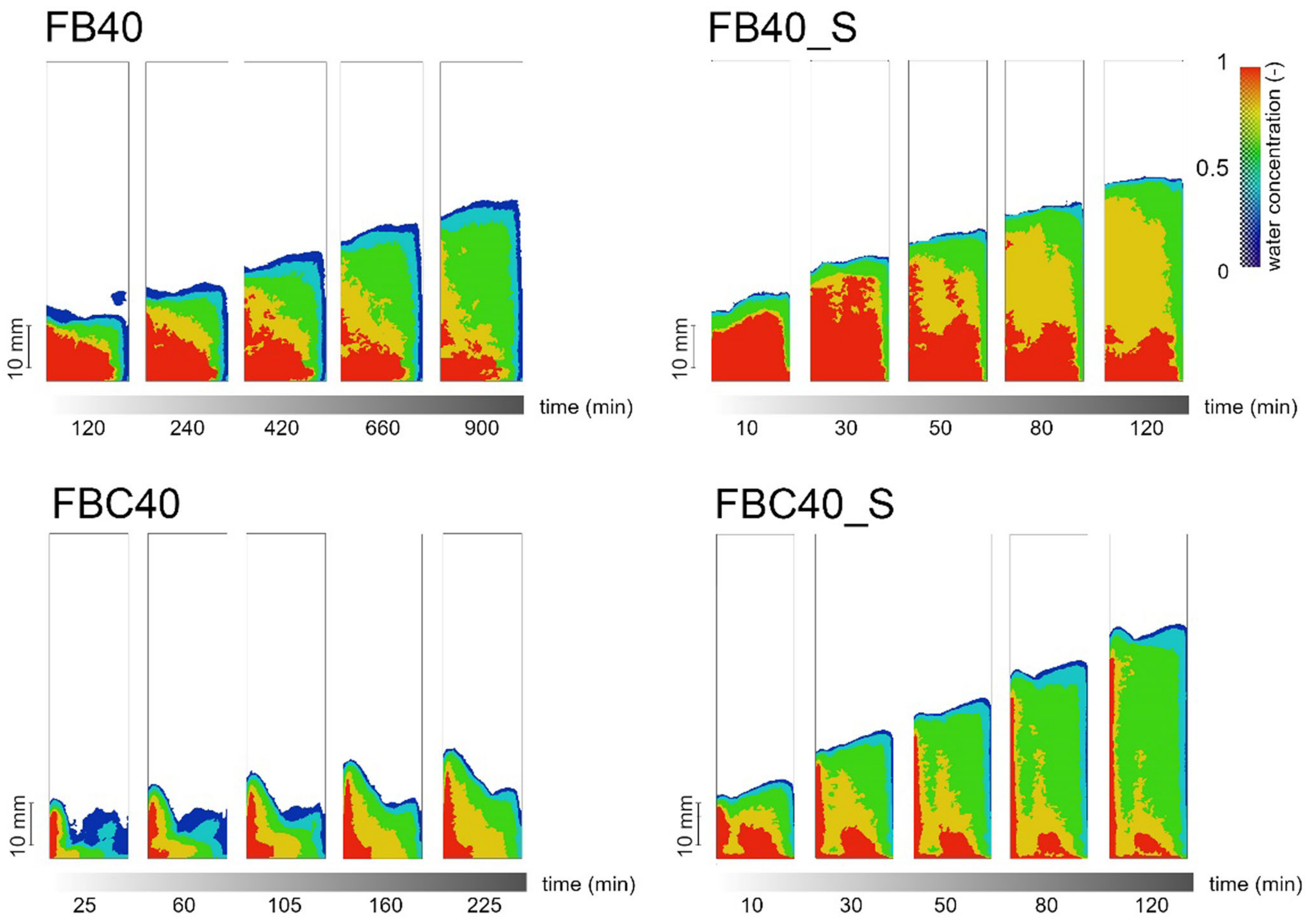

Fig. 5 Contour maps during water uptake of cutting sludges-based samples. At the bottom of each frame, the progression bar shows the time stamp selected. The colour map at the top right corner indicates the correspondence between the rendered colour and the relative concentration of water in the sample

Fig. 6 Water front position as a function of the square root of time for cutting sludges-based samples

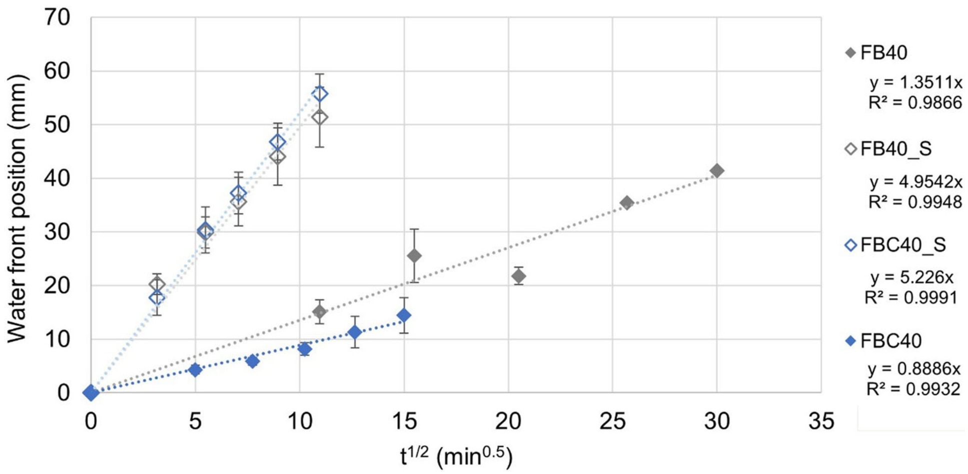

the material—in turn connected to an increase in compression strength values—[49, 50]; this causes a reduction in porosity and a consequent decrease in water entrance [50]. This formulation has been recently applied in a conservation intervention test on ancient pottery: the adjustment of the starting formulation with the Ca-rich additive guaranteed several advantages, such as the counteraction of the typical thixotropic behaviour of geopolymers, thus facilitating the creation of a Ca-rich hybrid geopolymeric network, and the improvement of the workability, increasing the plasticity of the slurry [40]. Here, we can confirm the advantages of this addition also in the optics of slower water absorption and, as a consequence, of chemical transfer and efflorescence formation.

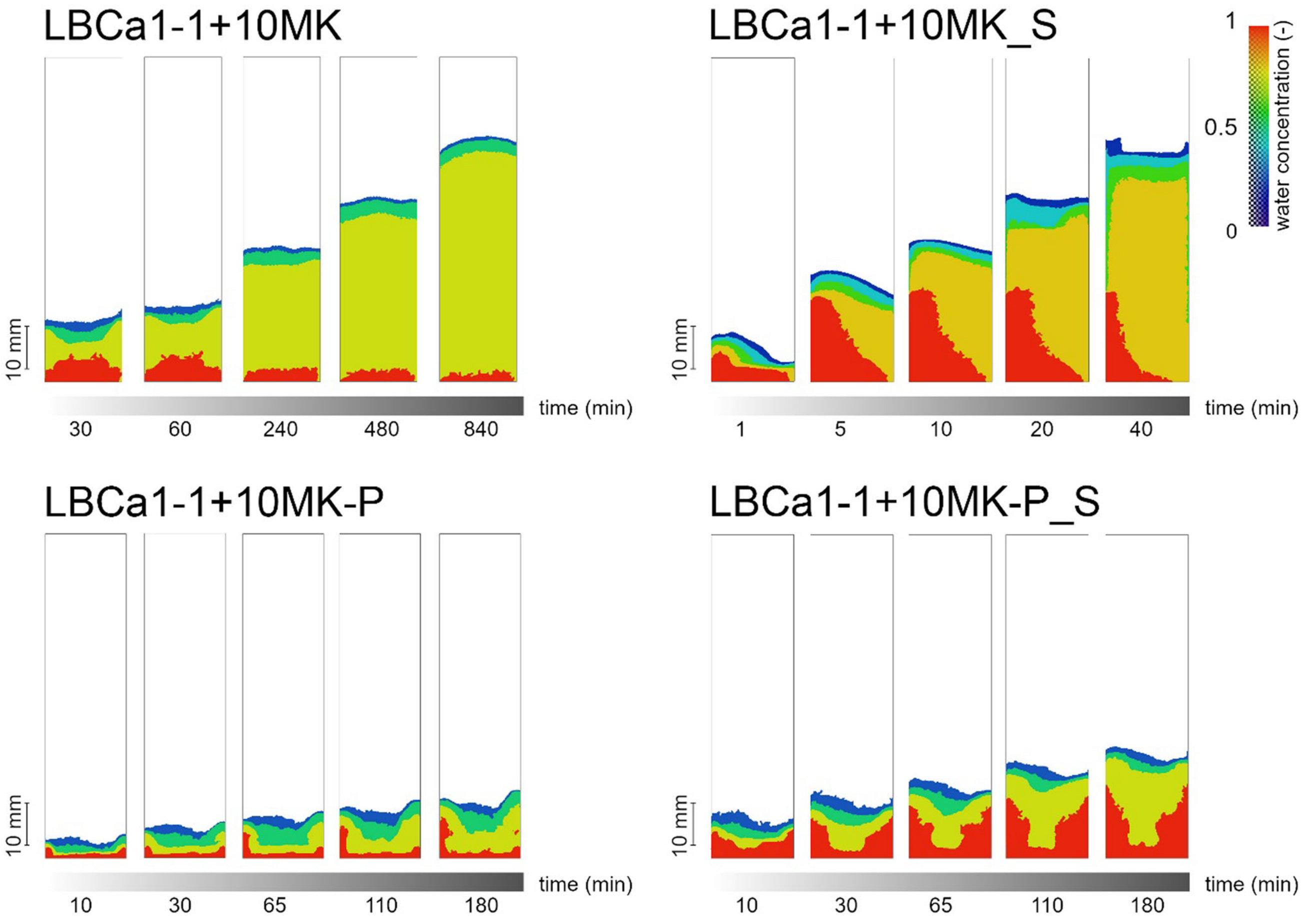

Fig. 7 Contour maps during water uptake of ceramic wastes-based samples. At the bottom of each frame, the progression bar shows the time stamp selected. The colour map at the top right corner indicates the correspondence between the rendered colour and the relative concentration of water in the sample

On the contrary, the reaction of LBCa1-1 + 10MK to salts crystallization is evidently strong. Furthermore, the high error indicates that the three replicates are not homogenous, contrarily to what found up to now for the other products. The high errors seem to be reconducted to the fact that, as revealed by previous studies on this specific formulation, prismatic structures with a (N,C)-A-S-H or C-A-S-H composition are formed, generating a discontinuity in the geopolymer matrix [34]. It can be hypothesized that these phases act as breaking points when salts crystallize, leading to the formation of cracks, partial disruption of the specimens and consequent very fast water uptake. The possible random formation of these structures in the matrix might therefore also explain the high error found on the three replicates.

3.2 Neutron tomography

In order to better observe the behaviour of the latter group of geopolymers, ceramic-based samples were subjected to neutron tomography after the imbibition experiment. The results are shown in Fig. 9. The cross sections highlight for sample LBCa 1–1 + 10MK_S an irregular uptake of water, due to the presence of fractures in the specimen, which explains both the high sorptivity and the high heterogeneity of the replicates for this sample, since fractures may form randomly in the specimens. For all the other samples, as already observed in radiographies, a symmetric rise of water is confirmed on the 3 dimensions. LBCa 1–1 + 10MK seems uniformly wet; LBCa 1–1 + 10MK-P shows the presence of water residues in the middle of the sample, probably due to the second imbibition necessary for tomography. The white spots can be attributed to voids above the water front and to closed porosities in the area below the water front.

Based on the reconstructed three-dimensional model obtained through the tomographic analysis, porosities were virtually extracted for the ceramic-based samples. Since the geopolymer matrix and porosities show a strong difference in neutron attenuation intensity—rendered as dark grey and white, respectively—these two components can be virtually separated through threshold segmentation. In the segmentation each pixel in the image slices composing the tomographic stack is assigned to a label which describes the region or material associated with the pixel (e.g. matrix or pore) based on its colour value. Then the properties and statistics of the segmented components can be calculated [45]. Therefore the total amount of pores was quantified as volume fraction and their shape was also

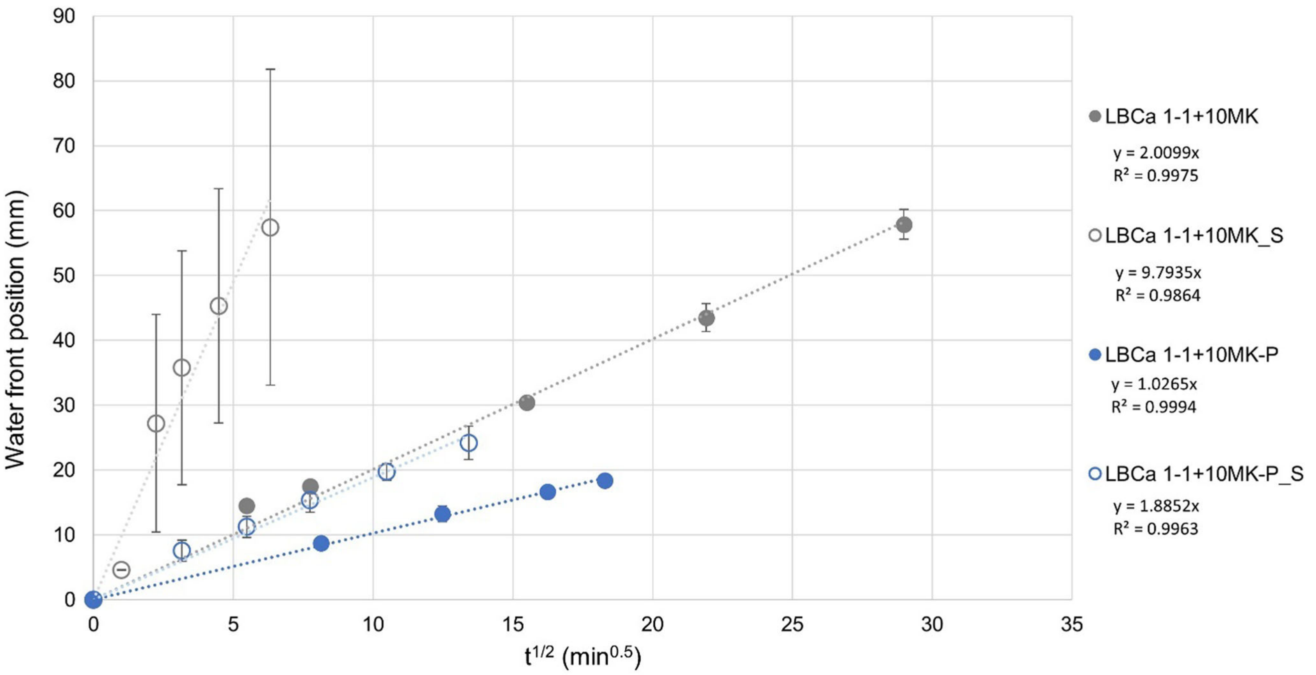

Fig. 8 Water front position as a function of the square root of time for ceramic waste-based samples

evaluated: (i) their three-dimensional volume; (ii) the Feret shape 3D, defined as D/d, where d is the minimum Feret diameter (one-dimensional measurement that estimates how "wide" an object is in a given direction) and D is the maximum Feret diameter in the orthogonal direction; (iii) the length 3D, the maximum of the Feret diameters, and (iv) the width 3D, the minimum of the Feret diameters (Table 2).

As expected, an increase in the total amount and a variation in the shape of pores were prominent in the weathered sample LBCa 1–1 + 10MK_S where the formation of cracks was observed (see the maximum Feret shape and length of the pores). Negligible variations were instead recorded for samples LBCa 1–1 + 10MK-P and LBCa 1–1 + 10MK-P_S. It is interesting to underline how the formulation with Prompt displays a higher percentage of pores visible through tomography (i.e. larger than 0.12 mm) (39.24%) with respect to the starting one (23.89%). This, together with the higher maximum volume, explains a slower capillary water uptake [20]. Here, the volume seems reduced after weathering, probably due to the occlusion caused by salts crystallization.

4 Discussions

Summarizing and comparing the behaviour of the different groups, it can be noticed that in all cases, the formulations adjusted with a calcium-rich additive show a slower progress of the wet front position with respect to the starting formulations. In all cases, except for ceramic group, the weathered geopolymers behave quite similarly independently from the presence or not of the additive or the fibres. The ceramic exception underlines the importance of the additive presence in this formulation in order to avoid undesired effects, addition that makes this product the slowest in water absorbance within the products here studied. Comparing the starting formulations, instead, the lowest sorptivity is that of the basalt cutting sludge geopolymer, that in fact is affected the least by the presence of the additive. In all cases, the salts crystallization test increases the sorptivity. The filling of pores with salts reduces their diameter and favours the capillary water uptake [20], and above all the formation of cracks, already observed for example for ceramic starting formulation, guarantees the rapid filling with water [13–15].

The mass difference before and after the whole weathering treatment has been calculated using the formula in (1) and is reported in Table 3 for each replicate of each sample. The mass difference is almost always negative, registering therefore an overall mass loss in the geopolymers, except for one sample, LBCa1-1 + 10MK-P, that gains weight: probably in this case, the filling of pores with salts is not compensated by the formation of cracks and loss of material. According to X-ray diffraction, [40], LBCa1-1 + 10MK-P is characterized by the presence of calcite and pirssonite ($Na_2Ca(CO_3)_2 \cdot 2H_2O$), that are not found in the respective starting formulation.

To confirm if the increase in sorptivity after weathering is connected to the mass difference, the mass loss was plotted against the slopes of the linear regressions of the weathered samples and the result is shown in Fig. 10. The big error connected to LBCa1-1 + 10MK_S stands out soon after noticing a correlation between the above-mentioned parameters. On the other hand, looking at Fig. 8,

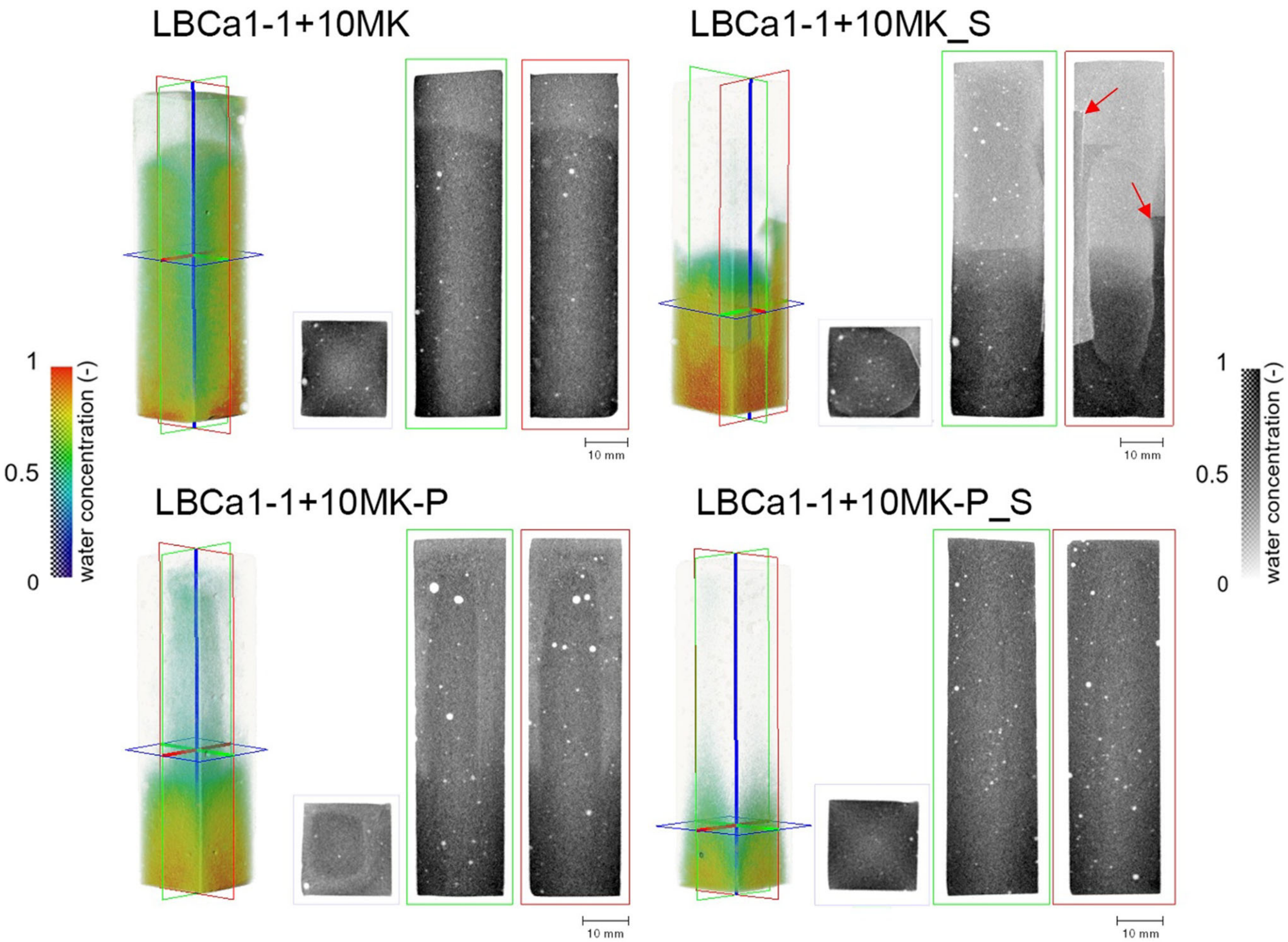

Fig. 9 On the left, three-dimensional model of the sample: the water is colour rendered while the sample surface is visualized in transparency. The neutron attenuation increases linearly with the water content, corresponding to the blue-yellow scalar. The red, green and blue frames indicate the orthogonal planes selected for the tomographic cross sections shown on the right side of the model in grey scale. The arrows indicate the fractures in LBCa1-1 + 10MK_S

Table 2 List of the different parameters for porosities for ceramic-based samples

	Pores	Volume3d (mm^3)			FeretShape3d			Length3d (mm)			Width3d (mm)		
	(%)	Av.	Min.	Max.	Av.	Min.	Max.	Av.	Min.	Max.	Av.	Min.	Max.
LBCa 1–1 + 10MK	23.89	0.0098	0.0010	1.1212	1.79	1.08	4.92	0.35	0.17	1.58	0.20	0.07	1.30
LBCa 1–1 + 10MK_S	62.37	0.0136	0.0010	3.4607	1.91	1.05	7.27	0.41	0.17	10.07	0.22	0.06	2.18
LBCa 1–1 + 10MK-P	39.24	0.0199	0.0010	6.2049	1.82	1.03	4.92	0.38	0.18	3.01	0.22	0.08	2.30
LBCa 1–1 + 10MK-P_S	40.25	0.0115	0.0010	2.7018	1.84	1.04	4.40	0.36	0.17	2.64	0.20	0.08	1.76

The volume percent of pores is reported for each sample; the Volume 3D represents the three-dimensional size of pores detected; the Feret shape 3D indicates the ratio D/d; the length 3D refers to the maximum of the Feret diameters, and the width 3D to the minimum of the Feret diameters. Average, minimum and maximum values are reported for each shape components

it is clear that the error on the front position would determine different sorptivity values, which could then be connected with the error on mass loss; therefore, the problem on this sample is strictly linked to the already discussed heterogeneity of the material.

5 Conclusions

With this work, thanks to neutron interaction with water, we were able to observe the behaviour of capillary water uptake in innovative green geomaterials synthesized to be tested in conservation of cultural heritage. We could distinguish the most advisable formulations as those less prone to aqueous solution transfer, bringing ions with consequent possible efflorescence formation. Different variables

Table 3 Mass difference after 15 cycles of NaCl crystallization calculated according to (1) for each replicate

Samples replicates	M_d (g)	M_f (g)	ΔM (%)
VM20_S 1	53.01	52.38	−1.19
VM20_S 2	54.43	53.70	−1.34
VM20_S 3	53.93	53.25	−1.28
VM20GR_S 1	55.03	54.53	−0.90
VM20GR_S 2	51.53	50.97	−1.09
VM20GR_S 3	51.84	51.26	−1.13
VM20CAR_S 1	56.84	56.15	−1.22
VM20CAR_S 2	58.42	57.91	−0.85
VM20CAR_S 3	57.40	56.89	−0.89
FB40_S 1	57.47	57.01	−0.80
FB40_S 2	56.32	55.89	−0.76
FB40_S 3	57.94	57.44	−0.85
FBC40_S 1	62.07	61.99	−0.14
FBC40_S 2	60.91	60.90	−0.02
FBC40_S 3	59.20	59.19	−0.03
LBCa1-1 + 10MK_S 1	53.32	53.03	−0.55
LBCa1-1 + 10MK_S 2	53.90	53.59	−0.58
LBCa1-1 + 10MK_S 3	51.36	48.01	−6.52
LBCa1-1 + 10MK-P_S 1	53.94	54.61	1.24
LBCa1-1 + 10MK-P_S 2	55.31	56.18	1.57
LBCa1-1 + 10MK-P_S 3	53.84	54.73	1.65

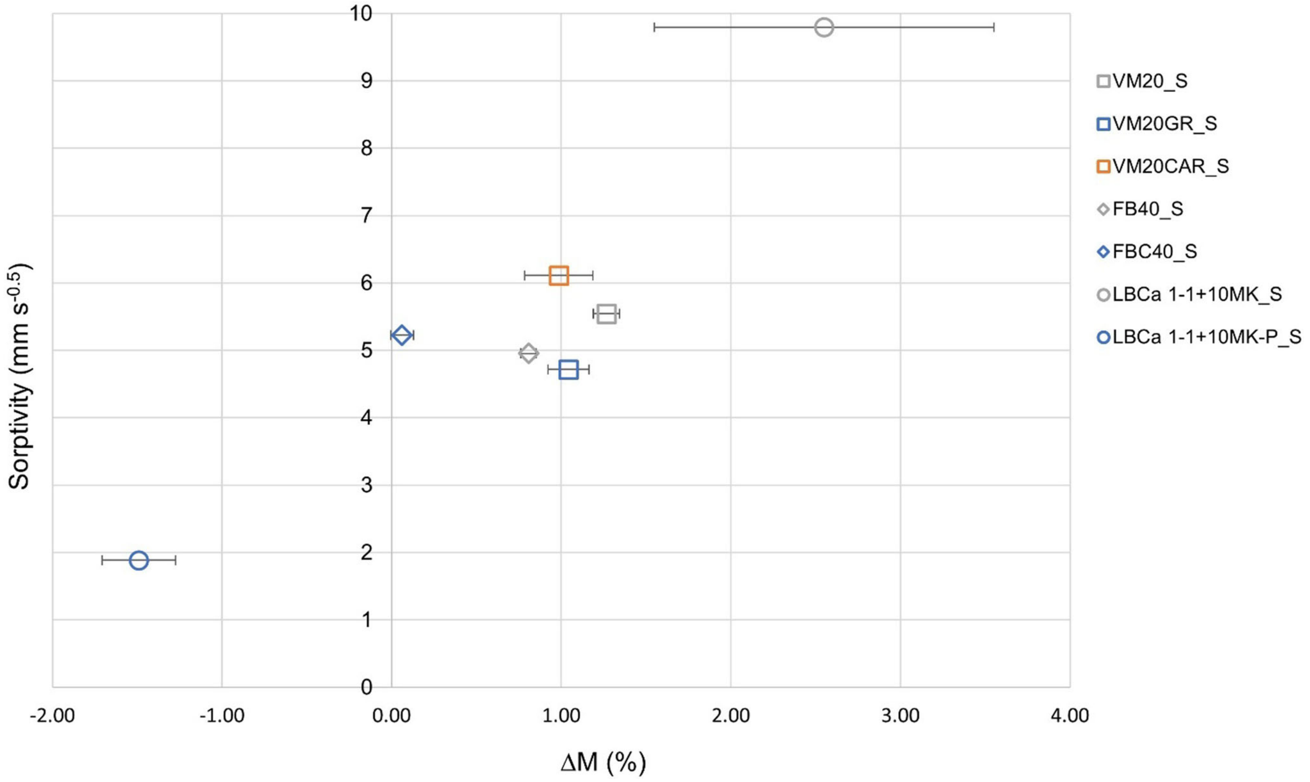

Fig. 10 Plot of the sorptivity obtained from the regression lines slopes Vs. the mass difference, expressed as mass loss, between the replicates before and after 15 cycles of NaCl crystallization

were evaluated such as the main precursors, Ca-based additives, carbon fibres addition, and resistance to salts crystallization. The conservation interventions carried out up to now with the resulting better formulation among ash and ceramics groups (i.e. those additivated with a Ca-bearing material) proved actually to be the most promising. The fruitful experience on the Monreale Cathedral site, for example, from which the addition of a small weight fraction of slake lime to volcanic ash base formulation originally took place, revealed winning also from the point of view of water uptake. The use of these formulations in new restoration applications, as well as that of basaltic cutting sludges even without Ca-based addition, is encouraged. As well, the good performance of the volcanic ash precursor coupled with carbon fibres reinforcing is promising and must be further analyzed. On the other hand, though showing a performance in the average of the other starting formulation, that based on ceramic waste is not advised, since its resistance to salts crystallization, an eventuality that must be taken into account when dealing with materials for conservation, is extremely low.

Acknowledgements LBC a.r.l. is thanked for providing and grinding ceramic residues. This work has been supported by 2017POCSI-CILIA1/5/5.4/9.2.3/AVV6.22/0001 (CUP G61I0002200095), EU-funded PON REACT (CUP E65F21002200005), and by MUR in the framework of PNRR Mission 4, Component 2, Investment 1.3 under project CHANGES. We gratefully acknowledge the Australian Nuclear Science and technology Organisation (ANSTO) for access to neutron beamtimes at the Australian Centre for Neutron Scattering (ACNS) (proposal P16134).

Funding Open access funding provided by Università degli Studi di Catania within the CRUI-CARE Agreement.

Data Availability Statement Data will be made available upon reasonable request.

Declarations

Conflict of interest The manuscript has associated data in a data repository "The authors have no competing interests to declare that are relevant to the content of this article".

References

1. C. Shi, B. Qu, J.L. Provis, Cem. Concr. Res. **122**, 227 (2019). https://doi.org/10.1016/j.cemconres.2019.05.009
2. A. Palomo, O. Maltseva, I. Garcia-Lodeiro, A. Fernández-Jiménez, Front. Chem. **9**, 705475 (2021). https://doi.org/10.3389/fchem.2021.705475
3. G. Barone, M.C. Caggiani, A. Coccato, C. Finocchiaro, M. Fugazzotto, G. Lanzafame, R. Occhipinti, A. Stroscio, P. Mazzoleni, IOP Conf. Ser: Mater. Sci. Eng. **777**, 012001 (2020). https://doi.org/10.1088/1757-899X/777/1/012001
4. M. Fugazzotto, R. Occhipinti, M.C. Caggiani, A. Coccato, C. Finocchiaro, G. Lanzafame, P. Mazzoleni, G. Nucatolo, G. Piacenti, S. Starinieri, A. Stroscio, G. Barone, Mater. Lett. **333**, 133626 (2023). https://doi.org/10.1016/j.matlet.2022.133626
5. R. Occhipinti, M.C. Caggiani, F. Andriulo, G. Barone, L. de Ferri, P. Mazzoleni, Mater. Lett. **315**, 131940 (2022). https://doi.org/10.1016/j.matlet.2022.131940
6. R. Occhipinti, M.C. Caggiani, L. de Ferri, Z. Xu, C.C. Steindal, J. Razavi, F. Andriulo, P. Mazzoleni, G. Barone, Ceram. Int. **49**, 21892 (2023). https://doi.org/10.1016/j.ceramint.2023.04.013
7. L. Srinivasamurthy, V.S. Chevali, Z. Zhang, M.A. Longhi, T.W. Loh, H. Wang, Constr. Build. Mater. **332**, 127273 (2022). https://doi.org/10.1016/j.conbuildmat.2022.127273
8. P. Zhang, F.H. Wittmann, P. Lura, H.S. Müller, S. Han, T. Zhao, Cem. Concr. Res. **108**, 152 (2018). https://doi.org/10.1016/j.cemconres.2018.03.003
9. A. El Abd, S.E. Kichanov, M. Taman, R.M. Nazarov, Constr. Build. Mater. **256**, 119471 (2020). https://doi.org/10.1016/j.conbuildmat.2020.119471
10. D.R.M. Brew, F.C. deBeer, M.J. Radebe, R. Nshimirimana, P.J. McGlinn, L.P. Aldridge, T.E. Payne, Nucl. Instrum. Meth. A 605 163 (2009). https://doi.org/10.1016/j.nima.2009.01.146.
11. C. Schröfl, V. Mechtcherine, A. Kaestner, P. Vontobel, J. Hovind, E. Lehmann, Constr. Build. Mater. **76**, 70 (2015). https://doi.org/10.1016/j.conbuildmat.2014.11.062
12. K. Van Tittelboom, D. Snoeck, P. Vontobel, F.H. Wittmann, N. De Belie, Mater. Struct. **46**(105), 1 (2013). https://doi.org/10.1617/s11527-012-9887-1
13. P. Zhang, F.H. Wittmann, T. Zhao, E.H. Lehmann, Physica B **405**, 1866 (2010). https://doi.org/10.1016/j.physb.2010.01.065
14. P. Zhang, F.H. Wittmann, T.J. Zhao, E.H. Lehmann, L. Tian, P. Vontobel, Nucl. Instrum. Meth. A **620**, 414 (2010). https://doi.org/10.1016/j.nima.2010.04.119
15. P. Zhang, F.H. Wittmann, T. Zhao, E.H. Lehmann, P. Vontobel, Nucl. Eng. Des. **241**, 4758 (2011). https://doi.org/10.1016/j.nucengdes.2011.02.031
16. P. Zhang, P. Wang, D. Hou, Z. Liu, M. Haist, T. Zhao, Cem. Concr. Compos. **78**, 13 (2017). https://doi.org/10.1016/j.cemconcomp.2016.12.006
17. A. El Abd, M. Taman, R.N. Behiry, M.R. El-Naggar, M. Eissa, W.A. Bar, T. Mongy, G.A. Mohammed, M.A. Hassan Amer, J. Build. Eng. 82, 107960 (2024). https://doi.org/10.1016/j.jobe.2023.107960.
18. A. El Abd, M. Taman, R.N. Behiry, M.R. El-Naggar, M. Eissa, A.M.A. Hassan, W.A. Bar, T. Mongy, M. Osman, A. Hassan, Bassem S. Nabawy, A.M. Rayan, Constr. Build. Mater. 449, 138436 (2024). https://doi.org/10.1016/j.conbuildmat.2024.138436.
19. H. Vu Tran, N. Gowripalan, P. De Silva, A. Paradowska, U. Garbe, P. Kidd, V. Sirivivatnanon, Cem. Concr. Compos. 114, 103759 (2020). https://doi.org/10.1016/j.cemconcomp.2020.103759.
20. S. Raneri, G. Barone, P. Mazzoleni, E. Rabot, Appl. Phys. A **122**, 969 (2016). https://doi.org/10.1007/s00339-016-0495-8
21. M. Ban, T. De Kock, F. Ott, G. Barone, A. Rohatsch, S. Raneri, Nanomater. **9**, 635 (2019). https://doi.org/10.3390/nano9040635
22. F. Hameed, B. Schillinger, A. Rohatsch, M. Zawisky, H. Rauch, Nucl. Instrum. Meth. A **605**, 150 (2009). https://doi.org/10.1016/j.nima.2009.01.139
23. M. Realini, C. Colombo, C. Conti, F. Grazzi, E. Perelli Cippo, J. Hovind, Anal. Bioanal. Chem. 409, 6133 (2017). https://doi.org/10.1007/s00216-017-0550-0.
24. M. Slavíková, F. Krejčí, P. Kotlík, J. Jakůbek, I. Tomandl, J. Vacík, Nucl. Instrum. Meth. B **338**, 42 (2014). https://doi.org/10.1016/j.nimb.2014.07.041
25. R. Ziel, A. Haus, A. Tulke, J. Membr. Sci. **323**, 241 (2008). https://doi.org/10.1016/j.memsci.2008.05.057

26. V. Cnudde, M.N. Boone, Earth-Sci. Rev. **123**, 1 (2013). https://doi.org/10.1016/j.earscirev.2013.04.003
27. C. Coletti, G. Cultrone, L. Maritan, C. Mazzoli, Mater Charact **121**, 82 (2016). https://doi.org/10.1016/j.matchar.2016.09.024
28. J. Dewanckele, T. De Kock, G. Fronteau, H. Derluyn, P. Vontobel, M. Dierick, L. Van Hoorebeke, P. Jacobs, V. Cnudde, Mater Charact **88**, 86 (2014). https://doi.org/10.1016/j.matchar.2013.12.007
29. G. Barone, C. Finocchiaro, I. Lancellotti, C. Leonelli, P. Mazzoleni, C. Sgarlata, A. Stroscio, Waste Biomass Valori. **12**, 1075 (2021). https://doi.org/10.1007/s12649-020-01004-6
30. C. Finocchiaro, G. Barone, P. Mazzoleni, C. Leonelli, A. Gharzouni, S. Rossignol, Constr. Build. Mater. **262**, 120095 (2020). https://doi.org/10.1016/j.conbuildmat.2020.120095
31. C. Finocchiaro, C.M. Belfiore, G. Barone, P. Mazzoleni, Ceram. Int. **48**, 36178 (2022). https://doi.org/10.1016/j.ceramint.2022.08.174
32. C. Finocchiaro, R. Occhipinti, G. Barone, P. Mazzoleni, F. Andreola, M. Romagnoli, C. Leonelli, Ceram. Int. **50**, 24479 (2024). https://doi.org/10.1016/j.ceramint.2024.04.181
33. S. Portale, C. Finocchiaro, R. Occhipinti, P. Mazzoleni, G. Barone, Mater. Lett. **333**, 133624 (2023). https://doi.org/10.1016/j.matlet.2022.133624
34. M. Fugazzotto, G. Cultrone, P. Mazzoleni, G. Barone, Ceram. Int. **49**, 9465 (2023). https://doi.org/10.1016/j.ceramint.2022.11.111
35. M. Fugazzotto, P. Mazzoleni, I. Lancellotti, R. Camerini, P. Ferrari, M.R. Tiné, I. Centauro, T. Salvatici, G. Barone, Minerals **13**, 815 (2023). https://doi.org/10.3390/min13060815
36. E.N. Kani, A. Allahverdi, J.L. Provis, Cem. Conc. Compos. **34**, 25 (2012). https://doi.org/10.1016/j.cemconcomp.2011.07.007
37. P. Garcés, J. Fraile, E. Vilaplana-Ortego, D. Cazorla-Amorós, E.G. Alcocel, L.G. Andión, Cem. Concr. Res. **35**, 324 (2005). https://doi.org/10.1016/j.cemconres.2004.05.013
38. H. Funke, S. Gelbric, L. Kroll, Fibers **4**, 11 (2016). https://doi.org/10.3390/fib4010011
39. S.H. Chu, H. Ye, L. Huang, L.G. Li, Constr. Build. Mater. **269**, 121278 (2021). https://doi.org/10.1016/j.conbuildmat.2020.121278
40. M. Fugazzotto, P. Mazzoleni, A. Stroscio, G. Barone, Sustainability **16**, 1085 (2024). https://doi.org/10.3390/su16031085
41. 12370 UNI-EN, Natural Stone Test Methods. Determination of Resistance to Salt Crystallization, 2020.
42. B. Lubelli, V. Cnudde, T. Diaz-Goncalves, E. Franzoni., R.P.J. van Hees, I. Ioannou, B. Menendez, C. Nunes, H. Siedel, M. Stefanidou, V. Verges-Belmin, H. Viles, Mater. Struct. 51, 55 (2018). https://doi.org/10.1617/s11527-018-1180-5.
43. U. Garbe, T. Randall, C. Hughes, G. Davidson, S. Pangelis, S.J. Kennedy, Phys. Procedia **69**, 27 (2015). https://doi.org/10.1016/j.phpro.2015.07.003
44. M. Dierick, B. Masschaele, V. Hoorebeke, Octopus, a Fast and User-friendly Tomographic Reconstruction Package Developed in LabView®. Meas. Sci. Technol. **15**, 1366 (2004). https://doi.org/10.1088/0957-0233/15/7/020
45. https://www.thermofisher.com/au/en/home/electron-microscopy/products/software-em-3d-vis/avizo-software.html
46. D. Zhang, Y. Wang, T. Zhang, Q. Yang, J. Build. Eng. **79**, 107883 (2023). https://doi.org/10.1016/j.jobe.2023.107883
47. T. Alomayri, H. Assaedi, F.U.A. Shaikh, I.M. Low, J. Asian Ceram. Soc. **2**, 223 (2014). https://doi.org/10.1016/j.jascer.2014.05.005
48. M. Ziada, S. Erdem, R.A. González-Lezcano, Y. Tammam, I. Unkar, Eng. Sci. Technol. Int. J. **46**, 101501 (2023). https://doi.org/10.1016/j.jestch.2023.101501
49. O. Mahmoodi, H. Siad, M. Lachemi, S. Dadsetan, M. Sahmaran, J. Build. Eng. **43**, 102906 (2021). https://doi.org/10.1016/j.jobe.2021.102906
50. E. Ozcelikci, A. Kul, M.F. Gunal, B.F. Ozel, G. Yildirim, A. Ashour, M. Sahmaran, J. Clean. Prod. **396**, 136522 (2023). https://doi.org/10.1016/j.jclepro.2023.136522